

Article

The Effects of Transition Metal Oxides (Me = Ti, Zr, Nb, and Ta) on the Mechanical Properties and Interfaces of B₄C Ceramics Fabricated via Pressureless Sintering

Guanqi Liu ¹, Shixing Chen ², Yanwei Zhao ³, Yudong Fu ^{1,*}  and Yujin Wang ²

¹ College of Materials Science and Chemical Engineering, Harbin Engineering University, Harbin 150001, China; liuguanqi@hrbeu.edu.cn

² School of Materials Science and Engineering, Harbin Institute of Technology, Harbin 150001, China; 19S009067@stu.hit.edu.cn (S.C.); wangyuj@hit.edu.cn (Y.W.)

³ Science and Technology on Advanced Functional Composite Laboratory, Aerospace Research Institute of Materials & Processing Technology, Beijing 100076, China; ywzh227@163.com

* Correspondence: fuyudong@hrbeu.edu.cn

Received: 10 November 2020; Accepted: 16 December 2020; Published: 18 December 2020



Abstract: There is little available research on how different transition metal oxides influence the behavior of B₄C-based ceramics, especially for Ta₂O₅ and Nb₂O₅. B₄C-MeB₂ (Me = Ti, Zr, Nb, and Ta) multiphase ceramic samples were prepared via in situ pressureless sintering at 2250 °C, involving the mixing of B₄C and MeO_x powders, namely TiO₂, ZrO₂, Nb₂O₅, and Ta₂O₅. The phase constituents, microstructures, and mechanical properties of the samples were tested. The results indicated that different transition metal elements had different effects on the ceramic matrix, as verified through a comparative analysis. Additionally, the doped WC impurity during the ball milling process led to the production of (Me, W)B₂ and W₂B₅, which brought about changes in morphology and performance. In this study, the Ta₂O₅-added sample exhibited the best performance, with elastic modulus, flexural strength, Vickers hardness, and fracture toughness values of 312.0 GPa, 16.3 GPa, 313.0 MPa, and 6.08 MPa·m^{1/2}, respectively. The comprehensive mechanical properties were better than the reported values when the mass fraction of the second phase was around five percent.

Keywords: pressureless sintering; boron carbide; transition metal oxide; multiphase ceramics

1. Introduction

Boron carbide (B₄C) is an essential structural ceramic due to its atomic structure. According to previous studies, the most notable properties of pure B₄C ceramic are its high melting point (2447 °C), extreme hardness (50 GPa), and low density (2.52 g/cm³) [1–3]. Although it exhibits attractive performance in various applications, the practical application of B₄C has been severely restricted as a result of its low fracture toughness and poor sinterability. These disadvantages are caused by the low self-diffusion coefficient and the dominance of covalent bonds in the B₄C atomic structure [4–8]. To solve this problem in order to improve the mechanical properties of multiphase ceramics, scholars and engineers have added various second-phase constituents [9–11].

According to previous research, the addition of IVB and VB transition metals, such as TiB₂, ZrB₂, NbB₂, and TaB₂, into the B₄C matrix can lead to densification and mechanical property improvements. These kinds of multiphase ceramics could be used as the initial bases for cutting tools, ballistic armor, thermal protection components, wear-resistant parts, and turbojet blades [12–15].

The conventional toughening methods used for B_4C typically involve laminated composite toughening, particle toughening, and whisker toughening [16,17]. Through whisker bridging, the whisker “pull-out” effect, and crack deformation, energy can be effectively consumed, thwarting crack propagation and improving the fracture toughness. For example, by adding 10 wt.% TiO_2 into B_4C at 1950 °C and 30 MPa, Wang et al. synthesized B_4C - TiB_2 composite ceramics with a relative density, flexural strength, and fracture toughness of 97.6%, 408.0 MPa, and 5.3 $MPa \cdot m^{1/2}$, respectively [18]. Tamari et al. prepared composite ceramics of B_4C containing up to 30 vol% SiC whiskers by hot pressing at 2000–2200 °C under 30 MPa for 30 min. The Vickers hardness and elastic modulus were 30 and 430 GPa, respectively [19]. Jiang et al. prepared B_4C /40%BN laminated ceramic composites via the hot pressing process at 1850 °C for 1 h under 30 MPa pressure, for which the flexural strength was 245 MPa and the fracture toughness was 3.52 $MPa \cdot m^{1/2}$ [20].

Compared with borides and carbides, oxides generate gas through in situ reactions with the matrix during the sintering process, meaning a uniform and refined structure can be obtained, resulting in materials with improved mechanical properties [21–25]. Although the addition of Ti, Zr, and other metal oxides to boron carbide has been extensively studied, transition metal oxides, including Ta and Nb, have not attracted much attention [26]. Moreover, no studies have been conducted that compare the effects of different transition metal oxides on boron carbide ceramics. Therefore, there is still space for further research in this direction.

Regarding the currently used sintering processes, the main methods include the hot press sintering method, spark plasma sintering (SPS) method, and pressureless sintering method [27–31]. Generally speaking, B_4C - TiB_2 composite ceramics possess a density of 98% when the temperature and pressure involved in the hot press sintering exceed 1957 °C and 30 MPa, respectively [32]. As for the spark plasma sintering method, a temperature of 1760 °C and pressure of 40 MPa are required to prepare materials of the same density [33]. Additionally, the preparation of B_4C - TiB_2 multiphase ceramics with pressureless sintering requires a temperature of more than 2150 °C [34]. Among the three methods, the hot press sintering method and spark plasma sintering method have stricter industrial production conditions, a more complicated process, and require more expensive equipment, with the required use of a mold being one of the other limitations. At the same time, hot press sintering synchronously involves more energy expenditure than the other two methods and results in increased inefficiency in industry. However, the cost of pressureless sintering is low and the operation method is simple, meaning products with complex shapes can be prepared, making this method suitable for mass production.

This study prepared B_4C - MeB_2 multiphase ceramics (Me = Ti, Zr, Nb, or Ta). For practical purposes, we chose to use the pressureless sintering method. We tested the mechanical properties and microstructures to determine how different transition metal oxides influence the behavior of B_4C - MeB_2 multiphase ceramics. The main aim of this project is to complement the existing research studies on B_4C - MeB_2 multiphase ceramics, with the results possibly providing useful references for further study.

2. Materials and Methods

2.1. Materials and Preparation

Table 1 shows the compositions of the samples used in this research. All of the B_4C - MeB_2 multiphase ceramics were fabricated by pressureless sintering at 2250 °C for 60 min under an Ar atmosphere, with a heating rate of 10 °C/min. The raw B_4C powder (Mudanjiang Diamond Boron Carbide Co., Ltd., Mudanjiang, China) used in this research had a purity of 98.5% and particle size of approximately 2.2–5 μm . The raw TiO_2 , ZrO_2 , Nb_2O_5 , and Ta_2O_5 powders (Changsha Weihui High-Tech New Materials Co., Ltd., Changsha, China) had purities of 98.5% and particle sizes of approximately 2 μm . The B_4C - MeB_2 ceramics were comprised of 95 wt.% B_4C +5 wt.% MeO_x (Me = Ti, Zr, Nb, and Ta). After high-energy ball milling (Pulverisette 4) at a rate of 200 r/min with a grinding media/material ratio of 10:1, the size of the mixed powders was less than 1 μm on average. The mixed

powders were dried and sieved through a 100-mesh screen in a flowing Ar atmosphere. Phenolic resin was added as molding binder.

Table 1. The starting compositions (in wt.%) and processing conditions of sintered compounds.

Sample	Composition (wt.%)		Preparation Conditions	
	B ₄ C	MeO _x	Temperature (°C)	Time (h)
B ₄ C	100	-		
B ₄ C + TiO ₂	95	5		
B ₄ C + ZrO ₂	95	5	2250	1
B ₄ C + Nb ₂ O ₅	95	5		
B ₄ C + Ta ₂ O ₅	95	5		

2.2. Experiments and Characterization

The Archimedes principle was used to measure the relative densities of the final samples. The phase constituents of the synthesized products were analyzed using X-ray diffraction (X'PERT, Panalytical, Almelo, The Netherlands) with Cu K α radiation. The surface structures and fracture surfaces of products were observed with a scanning electron microscope (SEM, Merlin Compact, Carl Zeiss, Rauenstein, Germany). The compositions were observed using an energy-dispersive X-ray spectroscopy system (Helios NanoLab, FEI, Hillsboro, OR, USA). Microhardness values were determined using a Vickers indentation tester (HVS-1000Z, Shanghai, China) with a diamond indenter load of 9.8 N for 15 s. Flexural strength was measured using the three-point flexural method (3 mm \times 4 mm \times 36 mm) with a span of 30 mm and a crosshead speed of 0.5 mm/min. The fracture toughness was measured using the single-edge notched beam method (2 mm \times 4 mm \times 22 mm) across a span of 16 mm and with a crosshead speed of 0.05 mm/min.

3. Results and Discussion

3.1. Thermodynamic Calculations

For the reactions in this study, the Gibbs free energy values were calculated using FactSage software (version 8.0). B₂O₃ usually bonds to the surfaces of B₄C particles, reacting with B₄C during the heating process and releasing gas. The fly-off from the gas inhibits densification. The reaction also causes grain growth during ceramic sintering. The reactions between B₄C and MeO_x involved in the sintering process are as follows:



We set up all of the reactions in order to find out how the phases change during the sintering process. Reactions (1)–(4) occur between B₄C and MeO_x (Me = Ti, Zr, Nb, and Ta), showing that all of the additives may cause in situ reactions. Reactions (5)–(6) are the reactions between the phenolic resin, as a carbon source, and residual B₂O₃ in the B₄C powder. The sintering densification was

promoted due to the consumption of oxide on the surface of the B_4C , which inhibited grain growth. Figure 1 displays the Gibbs free energy values from 500 to 2500 °C for all of the reactions, which were calculated using FactSage 8.0. These results were in accordance with thermodynamics theories—all of the reactions occurred in this process. The final products mainly included B_4C and MeB_2 phases (Me = Ti, Zr, Nb, and Ta).

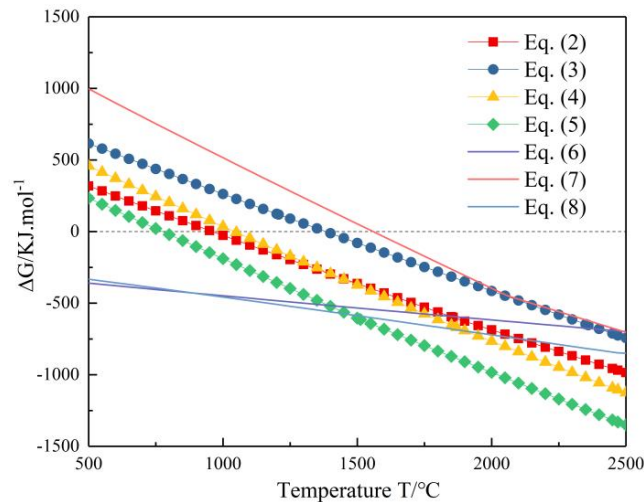


Figure 1. Gibbs free energy changes for each reaction as a function of temperature.

3.2. Phase Analysis

Figure 2 contains the XRD patterns of the final products, showing that the final samples were mainly composed of B_4C and MeB_2 . Meanwhile, some graphite was retained as a residue. W_2B_5 was also present in the ZrO_2 -added sample. The use of WC (Tungsten carbide) balls introduced some WC into the powder samples, which then reacted during sintering according to (7). The speculated WC was not found in the XRD patterns of samples, except in the ZrO_2 -added sample. Further analysis of the energy spectrum was needed. Compared with diffraction standard cards (shown as red lines), it was found that the diffraction peaks of the ZrO_2 -added, Nb_2O_5 -added, and Ta_2O_5 -added samples were shifted to higher angles, which may have been caused by W atoms migrating to the additive lattices to form (Me, W) B_2 solid solutions. Meanwhile, there were few transition metal oxides that were observed in the final products. The main phases of the final products were B_4C , (Me, W) B_2 , and graphite. This result indicates that B_4C - MeB_2 multiphase ceramics were successfully fabricated in this research.

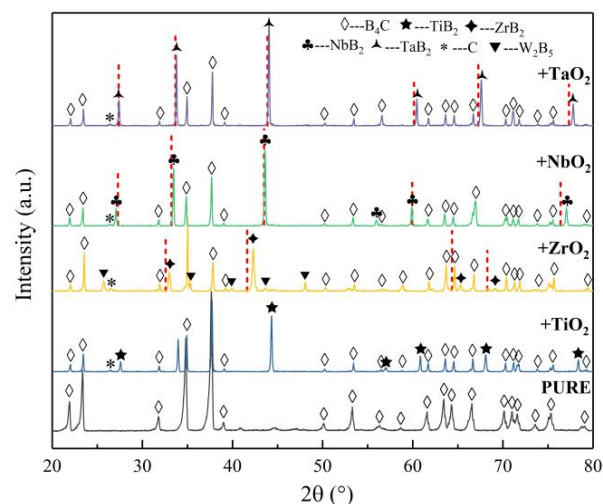


Figure 2. XRD pattern analysis for different sintered samples.

Table 2 shows the relative densities of the final products. The relative density of the pure sample was 78.3%. It can be clearly seen from the data in Table 1 that the addition of MeO_x significantly increased the samples' densification. Except for the TiO_2 -added sample (relative density of 89.3%), the relative densities of other B_4C - MeB_2 multiphase ceramics exceeded 93%.

Table 2. The relative densities of the different samples.

No.	Sample Name	Relative Density (%)
1	B_4C	78.3
2	$\text{B}_4\text{C}+5\%\text{TiO}_2$	89.3
3	$\text{B}_4\text{C}+5\%\text{ZrO}_2$	93.2
4	$\text{B}_4\text{C}+5\%\text{Nb}_2\text{O}_5$	93.8
5	$\text{B}_4\text{C}+5\%\text{Ta}_2\text{O}_5$	94.0

Figure 3 shows the microspheres of different samples through SEM images. Overall, the samples contained several pores. The main component of the second phase was the $(\text{Me}, \text{W})\text{B}_2$ solid solution. The resulting XRD patterns (Figure 2) and energy spectra (Figure 3) confirmed this. As shown in Figure 3a, the TiO_2 -added sample consisted of a dark grey matrix, as attributed to B_4C , with the light grey second phase as attributed to $(\text{Ti}, \text{W})\text{B}_2$. These second-phase particles were uniformly distributed but the number of pores was larger than in other particles. Additionally, the particle diameters for $(\text{Ti}, \text{W})\text{B}_2$ samples were smaller than those of other samples. Figure 3b shows that there is a small number of pores in the ZrO_2 -added sample, in which the light grey $(\text{Zr}, \text{W})\text{B}_2$ solid-solution phase and bright white W_2B_5 phase were evenly distributed. Figure 3c shows that the Nb_2O_5 -added sample exhibited a high density without distinct pores, in which the $(\text{Nb}, \text{W})\text{B}_2$ solid-solution phase can be observed as a white phase. Figure 3d shows the Ta_2O_5 -added sample, whose $(\text{Ta}, \text{W})\text{B}_2$ solid-solution second phase had a similar distribution to the $(\text{Nb}, \text{W})\text{B}_2$ solid-solution phase in the Nb_2O_5 -added sample.

3.3. Mechanical Properties

Table 3 shows the elastic modulus and Vickers hardness values for different samples compared with the reported values. Firstly, the TiO_2 -added and ZrO_2 -added final products performed better, showing high elastic modulus values (>367 GPa) and hardness values (>19 GPa). Importantly, despite its lower relative density, the hardness of the TiO_2 -added sample was only lower than that of the ZrO_2 -added sample. Combined with the SEM analysis, it can be seen that the second-phase grains of the TiO_2 -added sample were well distributed in the B_4C matrix. Therefore, although its density is low, the hardness of the TiO_2 -added sample is still considerable due to the effect of fine-grain strengthening. For the ZrO_2 -added sample, according to the shift in the XRD peaks, it can be seen that W is highly soluble in ZrB_2 . Therefore, a $(\text{Zr}, \text{W})\text{B}_2$ solid-solution phase was formed with a large W content. Due to the effect of solid-solution strengthening, the hardness of this sample was significantly improved, having the highest hardness value out of all samples.

Compared with the reference values in other reports, the hardness values of the samples in this experiment were similar to those obtained using SPS and hot press sintering and higher than those obtained using the pressureless method. This is related to the sintering method used and the form of the added compound. Although the temperature is the same as that used in other sintering methods, pressureless sintering lacks the energy provided by external mechanical pressure or electric currents, which may reduce the degree of densification. In addition, the in situ oxide reaction process releases gas, which eventually leads to more pores being formed in the material. Therefore, the hardness of the samples prepared in this study was expected to be slightly lower than the reference values. However, owing to the variable solubility and theoretical hardness of the second phase, the values obtained in this study were higher than expected.

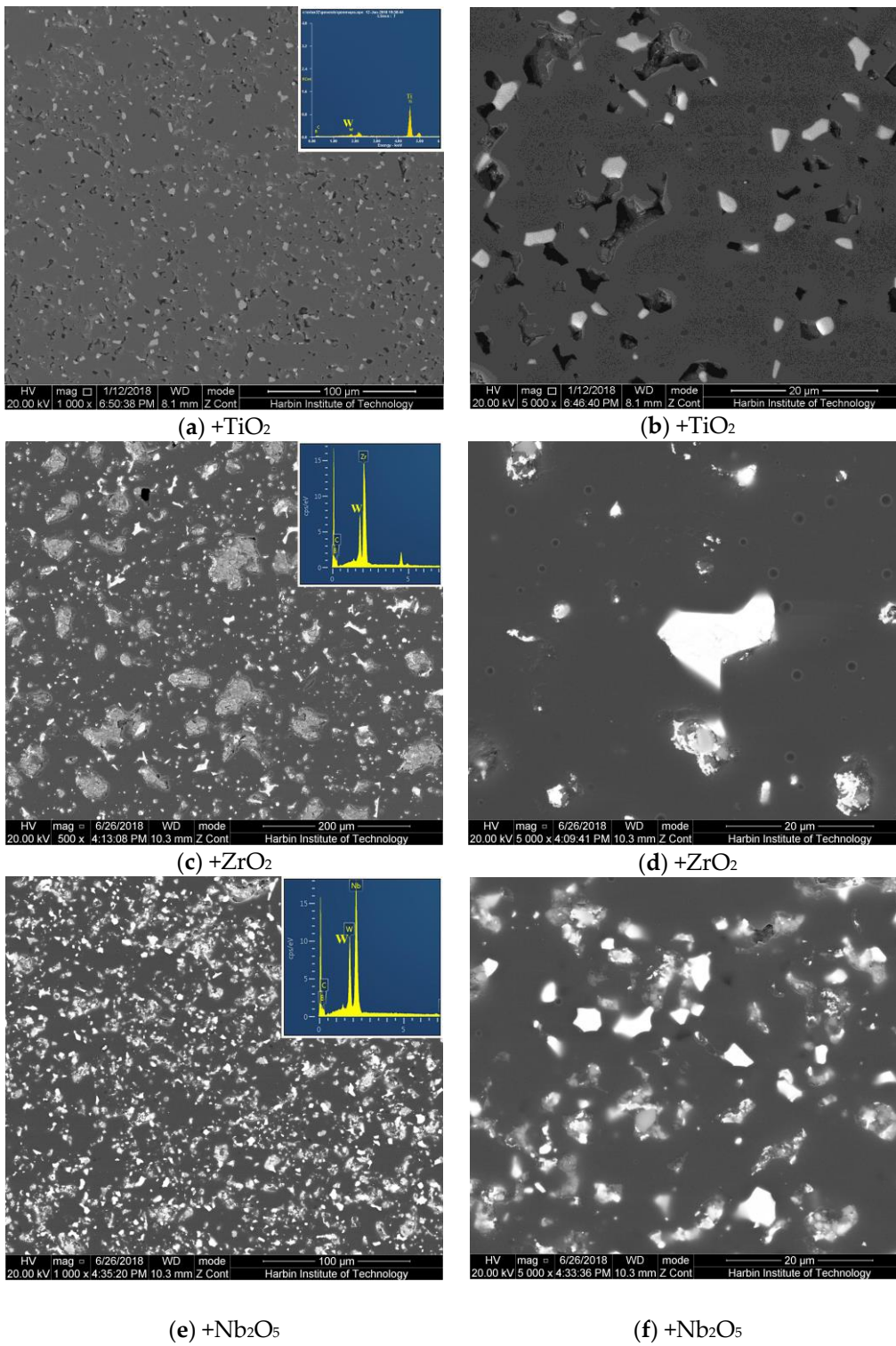


Figure 3. Cont.

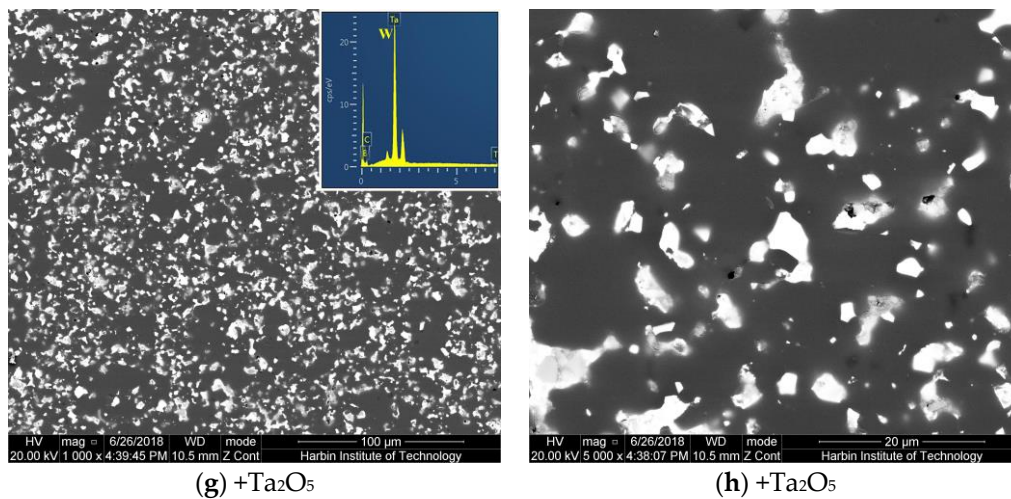


Figure 3. The magnification images of SEM analysis of B_4C - MeB_2 composites prepared from different additives (Me = Ti, Zr, Nb, or Ta): (a,b) + TiO_2 with different magnifications; (c,d) + ZrO_2 with different magnifications; (e,f) + Nb_2O_5 with different magnifications; (g,h) + Ta_2O_5 with different magnifications.

Table 3. Elastic modulus and Vickers hardness values for different samples as compared with the reported values [35–37].

No.	Process Condition		Sample Name	Elastic Modulus (GPa)	Hardness (GPa)
1			B_4C	209	12.4 ± 0.34
2			$B_4C + 5\%TiO_2$	411	19.2 ± 3.34
3	In this study	2250 °C, 1 h	$B_4C + 5\%ZrO_2$	367	21.1 ± 0.98
4			$B_4C + 5\%Nb_2O_5$	296	15.0 ± 2.27
5			$B_4C + 5\%Ta_2O_5$	312	16.3 ± 1.02
6	Xu et al. [35]	SPS, 1800 °C, 5 min, 50 MPa	$B_4C + 2.8\%TiB_2$	-	17
7	Dudina et al. [36]	SPS, 1700 °C, 2 min, 100 MPa	$B_4C + 23\%Ti$	-	19.5
9	Liu et al. [37]	2150 °C, 1 h	$B_4C + 5\%TiB_2$	-	17

Table 4 shows the flexural strength and fracture toughness of B_4C ceramics prepared in the study.

Table 4. Flexural strength and fracture toughness values for the different samples and the reported values [38–40].

No.	Process Condition		Samples Composition	Flexural Strength (MPa)	Fracture Toughness ($MPa \cdot m^{1/2}$)
1			B_4C	188 ± 4.38	1.98 ± 0.31
2			$B_4C + 5\%TiO_2$	336 ± 21.7	3.75 ± 0.30
3	In this study	2250 °C, 1 h	$B_4C + 5\%ZrO_2$	367 ± 24.9	4.06 ± 0.16
4			$B_4C + 5\%Nb_2O_5$	268 ± 15.3	5.56 ± 0.38
5			$B_4C + 5\%Ta_2O_5$	313 ± 11.7	6.08 ± 0.08
6	Wang et al. [18]	1850 °C, 1 h, 30 MPa	$B_4C + 10\%TiO_2$	260	3.3
7	Demirskyi et al. [38]	SPS, 1800 °C, 1 min, 2350 °C, 1 min, 20 MPa	$B_4C + 33\%TaB_2$	430	4.5
8	Liu et al. [39]	1600 °C, 1 h, 2060 °C, 0.5 h	$B_4C + 16\%ZrB_2$	320	3.1
9	Ho et al. [40]	2150 °C, 1 h	$B_4C + 5\%TiB_2$	260	2.6

The TiO_2 -added and ZrO_2 -added samples performed better in terms of flexural strength than the Nb_2O_5 -added and Ta_2O_5 -added samples, which was consistent with the elastic modulus and Vickers hardness. The fine crystals and solid solution led to the microstructure formation, which improved flexural strength. Owing to the lower relative density, the flexural strength of the TiO_2 -added sample did not reach that of the ZrO_2 -added sample.

In order to analyze the fracture mechanism of the material, we observed the microstructure morphology of the fractures through SEM images (as shown in Figure 4). The size and distribution of the second phase and the pores affected the mechanical properties of the samples. As shown in Figure 4a, the pores of the TiO₂-added samples had a uniform distribution. The second phase had an intergranular fracture mode and crystal grains were pulled out of the B₄C matrix. In the ZrO₂-added sample, the transgranular fracture in the B₄C matrix was effectively blocked by the ZrB₂ second-phase particles and pores. The transgranular fractures showed typical features, namely a river-like pattern, which can be clearly observed in Figure 4b (marked in yellow). The aggregation phenomenon was not observed in the distribution of pores. The pores in this sample were very small. Compared with large and aggregated pores, small pores led to a greater increase in the strength of the material. This was confirmed by the high flexural strength of the ZrO₂-added sample, as shown in Table 4. The fracture morphologies of the Nb₂O₅-added and Ta₂O₅-added samples are very similar. Compared with the former two samples, their B₄C matrix is denser. It is difficult to observe small and diffuse pores in the matrix (as shown in Figure 4c,d). Through analysis of the distribution of the second phase, it can be known that the second-phase particles had a “pinning effect” during the material fracture process, which is an excellent way to improve the flexural strength.

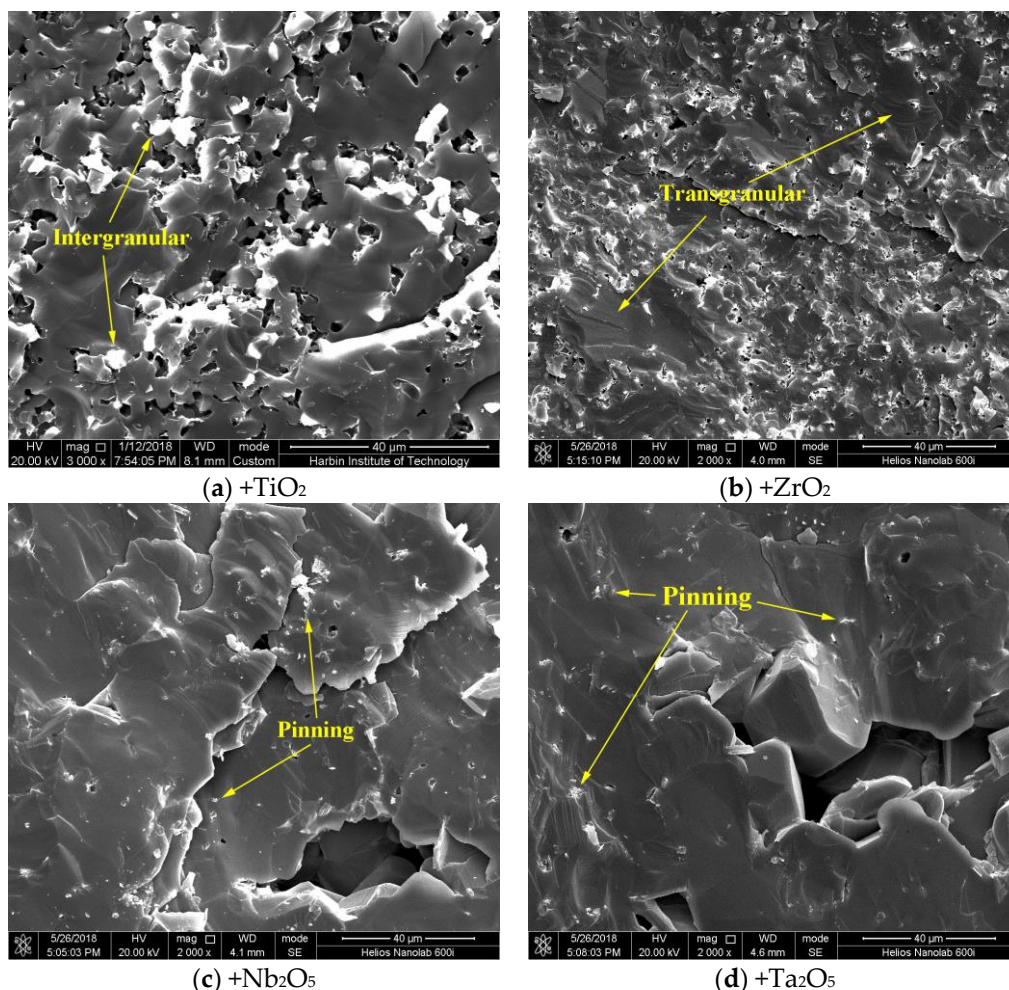


Figure 4. The results of SEM analysis of sintered samples and the fracture surfaces of final products: (a) +TiO₂; (b) +ZrO₂; (c) +Nb₂O₅; (d) +Ta₂O₅.

The average flexural strength of the multiphase-ceramics samples prepared in this study was 321 MPa, while the lowest value was above 260 MPa. Compared with the reference strength values for

pressureless sintering in the literature, the average strength value for the samples in this study was higher and was equivalent to those of hot press sintering samples.

One significant factor in the preparation of boron carbide ceramics is that they undergo toughening at high temperature. Therefore, it is necessary to find out how the final phase and microstructure influence the crack behavior. Figure 5 shows the crack propagation on the surfaces of the final samples after the hardness tests. In Figure 5a, crack bifurcation and deflection are apparent on the surface owing to significant aggregation among the second-phase particles of the TiO_2 -added product, in which the crack propagation is effectively hindered by energy consumption. Figure 5b shows the cracks on the surface of the ZrO_2 -added product, in which the crack deflection occurred without obvious presence of second-phase particles. This phenomenon can be analyzed using SEM images. In Figure 3b, the $(\text{Zr}, \text{W})\text{B}_2$ second-phase particles are large and unevenly distributed. The cracks could pass directly through the B_4C matrix instead of being deflected if they did not meet the second phase. However, the fine $(\text{Zr}, \text{W})\text{B}_2$ second-phase grains could cause strong crack deflection, making the addition of ZrO_2 an excellent to hinder crack propagation. In the SEM image of the Nb_2O_5 -added sample, shown in Figure 5c, the second-phase particles had a moderate particle size compared to the above products, which were also uniformly distributed in the B_4C matrix. Additionally, it is obvious that the Nb_2O_5 -added sample had higher fracture toughness owing to the crack deflection phenomenon. The morphology of the Ta_2O_5 -added final product was similar to the Nb_2O_5 -added final product according to Figure 5d. This was due to crack bifurcation, which hindered crack growth in both samples.

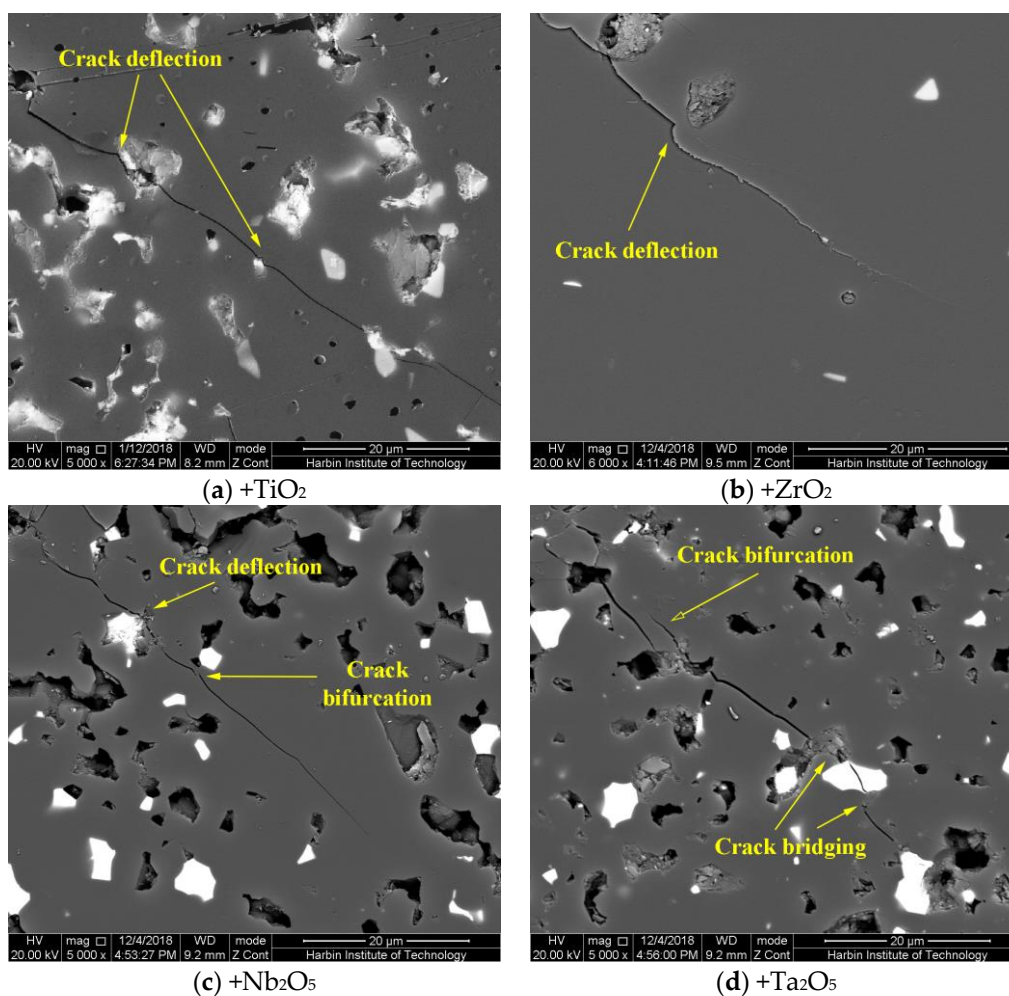


Figure 5. The results of SEM analysis of fracture surfaces and crack propagation of final products: (a) +TiO₂; (b) +ZrO₂; (c) +Nb₂O₅; (d) +Ta₂O₅.

The residual stresses were dispersed in the matrix around the second-phase particles. This phenomenon was always considered as the reason for the toughening of the composite ceramics. This kind of residual stress is, to a great extent, influenced by a mismatch in thermal expansion coefficients [41]. Different values mean that certain factors could induce microcracking behavior between the B_4C matrix and second-phase $(Me, W)B_2$ particles, which in turn could induce particle toughening.

The thermal expansion coefficient values for B_4C and the different MeB_x phases are shown in Table 5. Regarding Table 3, the CTE values of the second phases are higher than that of B_4C , except for in ZrB_2 . Owing to the bigger disparities among the thermal expansion coefficients of the samples with added transition metal oxides and that of the B_4C matrix, we speculate that the residual stress for TiB_2 , NbB_2 , and TaB_2 could be higher than that of the other final products. This conclusion was proven considering the data in Table 4 and Figure 5. Except for the TiO_2 -added sample, whose relative density was too low to reduce all of the mechanical properties, the Ta_2O_5 -added and Nb_2O_5 -added samples had a deflective crack path morphology and high fracture toughness. The thermal expansion coefficient mismatch between the B_4C matrix and the second phase MeB_2 or $(Me, W) B_x$ particles after the B_4C - MeB_2 polyphase ceramics were cooled down to room temperature resulted in the formation of residual stresses and microcracks. Second-phase particles with different thermal expansion coefficients can lead to differences in the residual stress among samples, which will affect the interface toughening during crack propagation.

Table 5. Comparison of thermal expansion coefficients (CTE) of boron carbide and the relevant transition metal borides [42,43].

Matter	B_4C	TiB_2	ZrB_2	NbB_2	TaB_2
CTE (ppm/K)	4.5	8.1	5.5	8.2	8.5

Additionally, the particle size, particle shape, particle orientation, surface energy, and interfacial bonding condition of the particles were determined to be the factors that could change the fracture toughness of the final products in this study. As shown in Figure 5, compared with the ZrO_2 -added product (Figure 5b), the rest of the samples performed better in terms of the average second-phase particle distribution and having suitable particle sizes. Such results could help explain the higher fracture toughness values of these samples, as detailed in Table 4. As for the Nb_2O_5 -added sample shown in Figure 5c, it can be seen that the crack was deflected rather than directly passing through upon encountering the second phase. This phenomenon could provide proof that the Nb_2O_5 additive had a significant second-phase toughening effect as it induced a high energy consumption. The fracture toughness of the Ta_2O_5 -added sample was found to be slightly larger than that of the Nb_2O_5 -added sample, whose cracks passed through the second phase. The energy from the crack propagation was largely consumed in this sample, with bifurcation and deflection occurring frequently. It was proven that Ta_2O_5 and Nb_2O_5 additives had a significant second-phase toughening effect.

The chemical reaction paths during the sintering process were similar in different B_4C - MeO_x samples. The pore distribution, particle size, and fracture modes were dependent on the metal oxide added ($Me = Ti, Zr, Nb, \text{ or } Ta$). The different final phases and reaction processes led to differences among the B_4C - MeB_2 ceramics. The mechanical properties of the MeO_x -added samples also varied significantly, since the mechanical properties are closely related to the final microstructure. Among all of the samples, the microtopography of the Ta_2O_5 -added sample stood out on the basis that it had the optimal mechanical properties. The B_4C - TaB_2 sample had good relative density and good distribution of the second phase, with a low number of pores. The fracture mode of this sample was a mixture of transgranular and intergranular fractures, in which the river-like patterns on the matrix and grain “pull-out” effect of the second-phase particles were observed. A significant toughening effect was caused by the evenly distributed second phase. Through the comprehensive analysis of the morphology and mechanical properties, it was seen that the second phase distribution of the B_4C - TaB_2 sample was uniform, and that the pores were fine and dispersed. The fine matrix

and second-phase particles formed the interface, enhancing the toughness and making this the best-performing sample of the three. Meanwhile, the performance of the Nb₂O₅-added sample was similar to the Ta₂O₅-added sample regarding the mechanical properties and micromorphology. It is worth mentioning that there are few academic publications covering B₄C-NbB₂ and B₄C-TaB₂ multiphase ceramics. However, the comprehensive performance of the samples in this research was considerable. For example, the structure of the interface between the second phase and the matrix and its effect on the microstructure and mechanical properties could be further studied by TEM (Transmission electron microscope). At the same time, it could be possible to improve performance by growing or coating the Nb or Ta compounds on the surface.

4. Conclusions

Little research is available on how different transition metal oxides influence the behavior of B₄C-based ceramics, especially for Ta₂O₅ and Nb₂O₅. It is of significance to find out the differences and rules among them. In this study, different transition metal oxides, such as TiO₂, ZrO₂, Nb₂O₅, and Ta₂O₅, were added to B₄C. The sintering process used was pressureless sintering at 2250 °C with 1 h holding time. By using FactSage software, the XRD pattern analysis shows that the reaction between B₄C and MeO_x is feasible, and then by measuring the relative density, SEM analysis, and measuring mechanical properties, the main conclusions are summarized. After adding MeO_x, the mechanical properties of boron carbide materials were observed to improve overall. Compared with other reports of B₄C ceramics, these ceramics have excellent properties. Among all of the investigated B₄C-MeB₂ multiphase ceramics, the main final phases are boron carbide and metal boride. Under the technological conditions of this study, all the samples have fine microstructure, few pores and uniformed second phase. B₄C-TaB₂ sample and B₄C-NbB₂ sample are due to the significant agglomeration of the second phase particles, and the crack deflection caused by the second phase grains led to the sample having better fracture toughness than others. The B₄C-TaB₂ sample had the most comprehensive properties. Its elastic modulus was 312.0 GPa, its hardness was 16.3 GPa, its flexural strength was 313.0 MPa, and its fracture toughness was 6.08 MPa·m^{1/2}. The Nb₂O₅-added sample performed similarly—the comprehensive mechanical properties were better than the reported values when the mass fraction of second phase was around 5%. B₄C-NbB₂ and B₄C-TaB₂ multiphase ceramics could highlight a new direction of research related to the microstructures and mechanical properties among boron carbide composite ceramics. For example, further studies could explore the different influences of Ta, TaB₂, and TaC on B₄C-based ceramics, and could also investigate the optimal solution needed to improve performance and study the mechanisms behind performance differences.

Author Contributions: Conceptualization, G.L. and Y.Z.; methodology, G.L.; software, S.C.; validation, Y.Z., Y.F., and Y.W.; formal analysis, G.L., S.C., and Y.W.; investigation, S.C.; resources, Y.F. and Y.W.; data curation, S.C.; writing—original draft preparation, G.L.; writing—review and editing, S.C.; visualization, Y.F.; supervision, Y.W.; project administration, Y.W. All authors have read and agreed to the published version of the manuscript.

Funding: This research was funded by the National Natural Science Foundation of China under Projection No.5187206.

Conflicts of Interest: The authors declare no conflict of interest.

References

1. Vas, N.; Lazzari, R.; Besson, J.M.; Baroni, S.; Corso, A.D. Atomic structure and vibrational properties of icosahedral α -boron and B₄C boron carbide. *Comp. Mater. Sci.* **2000**, *17*, 127–132.
2. Zorzi, J.E.; Perottoni, C.A.; Jornada, J.A.H.D. Hardness and wear resistance of B₄C ceramics prepared with several additives. *Mater. Lett.* **2005**, *59*, 2932–2935. [[CrossRef](#)]
3. Hayun, S.; Weizmann, A.; Dariel, M.P. Microstructural evolution during the infiltration of boron carbide with molten silicon. *J. Eur. Ceram. Soc.* **2010**, *30*, 1007–1014. [[CrossRef](#)]
4. With, G.D. High temperature fracture of boron carbide: Experiments and simple theoretical models. *J. Mater. Sci.* **1984**, *19*, 457–466. [[CrossRef](#)]

5. Bejarano, G.G.; Caicedo, J.C.; Prieto, P.; Balogh, A.G. Cutting tool performance enhancement by using a B₄C/BCN/C-BN multilayer system. *Phys. Status Solidi C* **2007**, *4*, 4282–4287. [[CrossRef](#)]
6. Sun, J.L.; Liu, C.X.; Liu, J.X. Effect of Grain Size on Erosion Wear of B₄C/TiC/Al₂O₃ Ceramic Nozzles. *Appl. Mech. Mater.* **2015**, *740*, 32–35. [[CrossRef](#)]
7. Guo, T.; Wang, C.; Dong, L.M.; Liang, T.X. Preparation and Properties of B₄C/Graphite Neutron Absorption Ball. *Key Eng. Mater.* **2014**, *602*, 248–251. [[CrossRef](#)]
8. Kumar, S.; Sairam, K.; Sonber, J.K.; Murthy, T.S.R.C.; Reddy, V.; Nageswara, G.V.S.; Srinivasa, T. Hot-pressing of MoSi₂ reinforced B₄C composites. *Ceram. Int.* **2014**, *40*, 16099–16105. [[CrossRef](#)]
9. Radev, D.; Avramova, I.; Kovacheva, D.; Gautam, D.; Radev, I. Synthesis of Boron Carbide by Reactive-Pulsed Electric Current Sintering in the Presence of Tungsten Boride. *Int. J. Appl. Ceram. Tec.* **2016**, *13*, 997–1007. [[CrossRef](#)]
10. Huang, S.; Kim, V.; Jozef, V. In-situ synthesis and densification of B₄C-(Zr, Ti)B₂ composites by pulsed electric current sintering. *J. Chinese Ceram. Soc.* **2014**, *1*, 113–121.
11. He, R.; Jing, L.; Qu, Z.; Zhou, Z.; Ai, S.; Kai, W. Effects of ZrB₂ contents on the mechanical properties and thermal shock resistance of B₄C-ZrB₂ ceramics. *Mater. Design* **2015**, *71*, 56–61. [[CrossRef](#)]
12. Zou, J.; Huang, S.G.; Vanmeensel, K.; Zhang, G.J.; Vleugels, J.; Vander-Biest, O. Spark Plasma Sintering of Superhard B₄C-ZrB₂ Ceramics by Carbide Boronizing. *J. Am. Ceram. Soc.* **2013**, *96*, 1055–1059. [[CrossRef](#)]
13. Zhang, X.R.; Zhang, Z.X.; Wang, W.X.; Che, H.W.; Zhang, X.L.; Bai, Y.M.; Zhang, L.; Fu, Z.G. Densification behaviour and mechanical properties of B₄C-SiC intergranular/intragranular nanocomposites fabricated through spark plasma sintering assisted by mechanochemistry. *Ceram. Int.* **2017**, *43*, 1904–1910. [[CrossRef](#)]
14. You, Y.; Tan, D.W.; Guo, W.M.; Wu, S.H.; Lin, H.T.; Luo, Z. TaB₂ powders synthesis by reduction of Ta₂O₅ with B₄C. *Ceram. Int.* **2017**, *43*, 897–900. [[CrossRef](#)]
15. Saeedi, H.M.; Baharvandi, H.R. Comparing the effects of different sintering methods for ceramics on the physical and mechanical properties of B₄C-TiB₂ nanocomposites. *Int. J. Refract. Met. H* **2015**, *51*, 224–232. [[CrossRef](#)]
16. Zhang, X.R.; Zhang, Z.X.; Wang, W.M.; Zhang, X.L.; Fu, Z.Y. Preparation of B₄C composites toughened by TiB₂-SiC agglomerates. *J. Eur. Ceram. Soc.* **2017**, *37*, 865–869. [[CrossRef](#)]
17. Husarova, I.O.; Potapov, O.M.; Solodkyi, I.V.; Bogomol, I.I. Production and Properties of B₄C-TiB₂ Composites with Isotropic Eutectic Microstructure. *Powder Metall. Met. Ceram.* **2018**, *57*, 209–214. [[CrossRef](#)]
18. Wang, G.F.; Zhang, J.H.; Zhang, C.; Zhang, K.F. Densification and Mechanical Properties of B₄C Based Composites Sintered by Reaction Hot-Pressing. *Key Eng. Mater.* **2010**, *434*, 24–27. [[CrossRef](#)]
19. Tamari, N.; Kobayashi, H.; Tanaka, T.; Kondoh, I.; Kose, S. Mechanical Properties of B₄C-SiC Whisker Composite Ceramics. *J. Ceram. Soc. Jpn.* **2010**, *98*, 1159–1163. [[CrossRef](#)]
20. Jiang, T.; Tian, C.C. Investigation of Microstructure and Thermal Shock Resistance of the B₄C/BN Composites Fabricated by Hot-Pressing Process. *Key Eng. Mater.* **2012**, *512*, 748–752. [[CrossRef](#)]
21. Yan, Z.; Liu, J.; Zhang, J.; Ma, T.; Li, Z.; Yan, Z.; Jie, L. Biomorphic silicon/silicon carbide ceramics from birch powder. *Ceram. Int.* **2011**, *37*, 725–730. [[CrossRef](#)]
22. Neuman, E.W.; Hilmas, G.E.; Fahrenholtz, W.G. Processing, microstructure, and mechanical properties of zirconium diboride-boron carbide ceramics. *Ceram. Int.* **2017**, *43*, 6942–6948. [[CrossRef](#)]
23. Neuman, E.W.; Brown-Shaklee, H.J.; Hilmas, G.E.; Fahrenholtz, W.G. Titanium diboride-silicon carbide-boron carbide ceramics with super-high hardness and strength. *J. Am. Ceram. Soc.* **2017**, *101*, 497–501. [[CrossRef](#)]
24. Liu, L.; Geng, G.; Jiang, Y.; Wang, Y.; Hai, W.; Sun, W.Z.; Chen, Y.H.; Wu, L. Microstructure and mechanical properties of tantalum carbide ceramics: Effects of Si₃N₄ as sintering aid. *Ceram. Int.* **2017**, *43*, 5136–5144. [[CrossRef](#)]
25. Zhang, C.; Gupta, A.; Seal, S.; Boesl, B.; Agarwal, A. Solid solution synthesis of tantalum carbide-hafnium carbide by spark plasma sintering. *J. Am. Ceram. Soc.* **2017**, *100*, 1853–1862. [[CrossRef](#)]
26. Zhang, W.; Yamashita, S.J.; Kita, H. Progress in pressureless sintering of boron carbide ceramics—A review. *Adv. Appl. Ceram.* **2019**, *118*, 222–239. [[CrossRef](#)]
27. Gao, D.; Jing, J.; Yu, J.; Guo, X.; Zhang, Y.; Gong, H.; Zhang, Y. Graphene platelets enhanced pressureless sintered B₄C ceramics. *Roy. Soc. Open Sci.* **2018**, *5*, 171837. [[CrossRef](#)]
28. Moshtaghioun, B.M.; Diego, G.G.; Arturo, D.R. High-temperature plastic deformation of spark plasma sintered boron carbide-based composites: The case study of B₄C-SiC with/without graphite (g). *J. Eur. Ceram. Soc.* **2016**, *36*, 1127–1134. [[CrossRef](#)]

29. Ariza Galván, E.; Montealegre-Meléndez, I.; Arévalo, C.; Kitzmantel, M.; Neubauer, E. Ti/B₄C Composites Prepared by In Situ Reaction Using Inductive Hot Pressing. *Key Eng. Mater.* **2017**, *742*, 121–128. [[CrossRef](#)]
30. Sairam, K.; Vishwanadh, B.; Sonber, J.K.; Murthy, T.S.R.C.; Majumdar, S.; Mahata, T.; Basu, B. Competition between densification and microstructure development during spark plasma sintering of B₄C-Eu₂O₃. *J. Am. Ceram. Soc.* **2017**, *101*, 2516–2526. [[CrossRef](#)]
31. Perevislov, S.N.; Lysenkov, A.S.; Vikhman, S.V. Effect of Si additions on the microstructure and mechanical properties of hot-pressed B₄C. *Inorg. Mater.* **2017**, *53*, 376–380. [[CrossRef](#)]
32. Yue, X.Y.; Zhao, S.M.; Yu, L.; Ru, H.Q. Microstructures and Mechanical Properties of B₄C-TiB₂ Composite Prepared by Hot Pressure Sintering. *Key Eng. Mater.* **2010**, *434*, 50–53. [[CrossRef](#)]
33. Uygun, B.; Göller, G.; Onüralp, Y.; Şahin, F.Ç. Production and Characterization of Boron Carbide-Titanium Diboride Ceramics by Spark Plasma Sintering Method. *Adv. Sci. Technol.* **2010**, *63*, 68–73. [[CrossRef](#)]
34. Baharvandi, H.R.; Hadian, A.M.; Alizadeh, A. Processing and Mechanical Properties of Boron Carbide-Titanium Diboride Ceramic Matrix Composites. *Appl. Compos. Mater.* **2006**, *13*, 191–198. [[CrossRef](#)]
35. Xu, C.; Cai, Y.; Lodström, K.; Li, F.Z.; Esmailzadeh, S.; Zhang, G.-J. Spark plasma sintering of B₄C ceramics: The effects of milling medium and TiB₂ addition. *Int. J. Refract. Met. Hard Mater.* **2012**, *30*, 39–144. [[CrossRef](#)]
36. Dudina, D.V.; Hulbert, D.M.; Jiang, D.; Unuvar, C.; Cytron, S.J.; Mukherjee, A.K. In situ boron carbide-titanium diboride composites prepared by mechanical milling and subsequent spark plasma sintering. *J. Mater. Sci.* **2008**, *43*, 3569–3576. [[CrossRef](#)]
37. Liu, A.D.; Qiao, Y.J.; Liu, Y.Y. Pressureless sintering and properties of boron carbide-titanium diboride composites by in situ reaction. *Key Eng. Mater.* **2013**, *525*, 321–324. [[CrossRef](#)]
38. Demirskiy, D.; Sakka, Y.; Vasylykiv, O. High-Strength B₄C-TaB₂ Eutectic Composites Obtained via In Situ by Spark Plasma Sintering. *J. Am. Ceram. Soc.* **2016**, *99*, 2436–2441. [[CrossRef](#)]
39. Liu, R.; Ru, H.Q.; Zhao, Y.; Tang, D. In situ synthesis of B₄C ceramics toughened by ZrB₂ particles. *Chin. J. Mater. Res.* **2006**, *20*, 611–616.
40. Ho, C.J.; Tuan, W.H. Toughening and strengthening zirconia through the addition of a transient solid solution additive. *J. Eur. Ceram. Soc.* **2012**, *32*, 335–341. [[CrossRef](#)]
41. Liu, G.Q.; Chen, S.X.; Zhao, Y.W.; Fu, Y.D.; Wang, Y.J. The effect of transition metal carbides MeC (Me = Ti, Zr, Nb, and W) on mechanical properties of B₄C ceramics fabricated via pressureless sintering. *Ceram. Int.* **2020**, *46*, 27283–27291. [[CrossRef](#)]
42. Awaji, H.; Choi, S.M.; Yagi, E. Mechanisms of toughening and strengthening in ceramic-based nanocomposites. *Mech. Mater.* **2002**, *34*, 411–422. [[CrossRef](#)]
43. Vahldiek, F.W. Electrical resistivity, elastic modulus, and debye temperature of titanium diboride. *J. Less Common Met.* **1967**, *12*, 202–209. [[CrossRef](#)]

Publisher's Note: MDPI stays neutral with regard to jurisdictional claims in published maps and institutional affiliations.



© 2020 by the authors. Licensee MDPI, Basel, Switzerland. This article is an open access article distributed under the terms and conditions of the Creative Commons Attribution (CC BY) license (<http://creativecommons.org/licenses/by/4.0/>).